

The mass of dusty clumps with temperature and density structure

R. Cesaroni

INAF, Osservatorio Astrofisico di Arcetri, Largo E. Fermi 5, I-50125 Firenze, Italy e-mail: cesa@arcetri.astro.it

Received date / Accepted date

ABSTRACT

We consider a dusty clump in the two cases of spherical and cylindrical symmetry to investigate the effect of temperature and density gradients on the observed flux density. Conversely, we evaluate how the presence of such gradients affects the calculation of the clump mass from the observed flux. We provide the reader with approximate expressions relating flux density and mass in the optically thick and thin limits, in the Rayleigh-Jeans regime, and discuss the reliability of these expressions by comparing them to the outcome of a numerical code. Finally, we present an application of our calculations to three examples taken from the literature, which shows how the correction introduced after taking into account temperature and density gradients may affect our conclusions on the stability of the clumps.

Key words. radiation mechanisms: thermal – radiative transfer – methods: analytical – dust, extinction – radio continuum: ISM

1. Introduction

Estimating the mass of molecular, dusty clumps is of great importance for a number of reasons, such as the determination of the clump mass function, the calculation of the virial parameter, the estimate of molecular abundances, etc.. While various methods can be used for this purpose, the most common takes advantage of the fact that the spectral energy distribution (SED) of the continuum emission from a dusty, homogeneous, isothermal cloud can be approximated as a modified black-body. In this case, the emission at sufficiently long wavelengths is optically thin and the integrated flux density can be easily expressed as a function of the mass and temperature of the dust. For a given gas-to-dust mass ratio, this allows to derive the total mass of the cloud from the flux density, if the dust temperature and absorption coefficients are known. In practice, the cloud mass is evaluated as described in the pioneering study of Hildebrand (1983) and can be expressed as (see e.g. Eq. (1) of Schuller et al. 2009)

$$M = \frac{S_\nu d^2 \mathcal{R}}{\kappa(\nu) B_\nu(T)} \quad (1)$$

where S_ν is the flux density, d the distance to the cloud, B_ν the Planck function, T the dust temperature, κ the dust absorption coefficient per unit mass, and \mathcal{R} the gas-to-dust mass ratio.

While this simplified expression is perfectly adequate to most purposes, real life is much more complicated. Observations are currently performed at higher and higher frequencies, e.g. from space with the Herschel Space Observatory and from ground with the Atacama Large Millimeter and submillimeter Array (ALMA) which is now operative up to 900 GHz. At such bands dust optical depth cannot be neglected a priori and should be considered when converting flux density into mass. Also, compact molecular cores can be heated from outside (due to nearby luminous stars) or inside (due to embedded forming stars), which generates temperature gradients that in turn break

the assumption of isothermal clump. Density gradients are likely present too, owing to collapse during the star formation process or other phenomena (e.g. expansion in molecular outflows).

Additional sources of uncertainty on the estimate of the mass are related to the error on the flux measurement, the distance of the source (often poorly known), and the value of the dust absorption coefficient, which depends on the properties of the dust grains (see e.g. Ossenkopf & Henning 1994). The combination of all these errors may overcome the error caused by the assumptions of low optical depth and constant temperature. However, in some cases one is interested in quantities that do not depend on distance (e.g. the mass-to-luminosity ratio) or all targets are located basically at the same distance (as in studies of the core mass function within the same molecular cloud), which makes the distance error irrelevant. In addition, for other quantities, such as the virial parameter, it is important to determine whether the value lies above a given threshold and is thus useful to improve on the accuracy of the estimated parameter as much as possible. Neglecting the opacity as well as the temperature and density gradients may lead to wrong conclusions in these cases.

The goal of our study is to quantify the effects of large dust opacity and temperature and density gradients on the clump mass estimated with Eq. (1). In particular, in Sect. 2 we analyse the case of a spherically symmetric clump with temperature and density varying as power laws of the radius, in Sect. 3 we repeat the same exercise for a cylindrically symmetric clump and in Sect. 4 we apply the corrections estimated with our method to data from the literature. Finally, the results are summarized in Sect. 5.

2. Flux density of spherical clump

We want to calculate the integrated flux density emitted by the dust in a spherically symmetric clump. In our model the gas and dust are distributed between an inner radius R_i and an outer radius R_o , and the mass ratio between gas and dust, \mathcal{R} , does not depend on the radius, R . The dust temperature and density are

Send *offprint requests* to: R. Cesaroni, e-mail: cesa@arcetri.astro.it

expressed as

$$T = T_0 \left(\frac{R}{R_0} \right)^q \quad (2)$$

$$\rho = \rho_0 \left(\frac{R}{R_0} \right)^p \quad (3)$$

where T_0 and ρ_0 are the dust temperature and density at the outer radius. By definition, the gas density is equal to $\rho \mathcal{R}$.

2.1. Approximate analytical expression

As a first step, it is instructive to calculate the expression of the integrated flux density in the optically thin and thick limits. In the latter, only the photons emitted from the clump surface contribute to the observed flux, which is given by

$$S_\nu = \frac{\pi B_\nu(T_0) 4\pi R_0^2}{4\pi d^2} = \Omega_0 B_\nu(T_0) \quad (4)$$

with $\Omega_0 = \pi R_0^2/d^2$ solid angle subtended by the clump. In practice such a thick limit can hardly be reached at (sub)millimeter wavelengths. This can be seen by estimating the density needed to achieve a dust opacity of 1 in a thin surface layer of thickness, e.g., $\Delta R = 0.1 R_0$. It is easy to show that the condition $\tau = \kappa \rho_0 \Delta R = 1$ in the template case $p = 0$ and $r_i = 0$ can be re-written as

$$\Sigma = \frac{4}{3} \frac{\mathcal{R} R_0}{\kappa \Delta R} \quad (5)$$

where $\Sigma = (4/3)\mathcal{R}\rho_0 R_0$ is the mean surface density of the clump. At 1 mm $\kappa \approx 1 \text{ cm}^2 \text{ g}^{-1}$ (see Ossenkopf & Henning 1994) and for $\mathcal{R} = 100$ one obtains $\Sigma \approx 10^3 \text{ g cm}^{-2}$, as opposed to $\Sigma \lesssim 1 \text{ g cm}^{-2}$ of typical molecular clumps.

In the optically thin limit, instead, all photons emitted by the grains freely escape from the clump and S_ν is obtained from

$$S_\nu = \frac{1}{4\pi d^2} \int_{R_i}^{R_0} 4\pi j_\nu 4\pi R^2 dR = \frac{4\pi}{d^2} \int_{R_i}^{R_0} \kappa \rho B_\nu R^2 dR \quad (6)$$

where j_ν is the dust emissivity and we made use of Kirchhoff's law $j_\nu/\kappa = B_\nu(T)$. If $h\nu \ll kT$ (with k Boltzmann constant and h Planck constant), this equation can be re-written using the Rayleigh-Jeans (hereafter RJ) approximation:

$$\begin{aligned} S_\nu &\approx \frac{4\pi}{d^2} \kappa \rho_0 \frac{2k\nu^2}{c^2} T_0 \int_{R_i}^{R_0} R^2 \left(\frac{R}{R_0} \right)^{q+p} dR \\ &= \frac{4\pi R_0^3}{d^2} \kappa \rho_0 \frac{2k\nu^2}{c^2} T_0 \int_{r_i}^1 r^{q+p+2} dr \end{aligned} \quad (7)$$

where we have defined $r = R/R_0$ and $r_i = R_i/R_0$.

One can relate the expression of S_ν to the mass of the clump, M . The latter can be computed from

$$M = \int_{R_i}^{R_0} \rho \mathcal{R} 4\pi R^2 dR = 4\pi R_0^3 \rho_0 \mathcal{R} \int_{r_i}^1 r^{p+2} dr. \quad (8)$$

From this expression and Eq. (7), one obtains

$$S_\nu = \frac{\kappa M}{\mathcal{R} d^2} \frac{2k\nu^2}{c^2} T_0 \frac{\int_{r_i}^1 r^{q+p+2} dr}{\int_{r_i}^1 r^{p+2} dr} = m \frac{2k\nu^2}{c^2} T_0 F(r_i; q, a) \quad (9)$$

where we have defined $m = \kappa M/(\mathcal{R} d^2)$, $a = p + 3$, and $F = \int_{r_i}^1 r^{q+a-1} dr / \int_{r_i}^1 r^{a-1} dr$. It is straightforward to demonstrate that function F takes the following values:

$$F = \begin{cases} 1 & \Leftrightarrow q = 0 \\ \frac{r_i^q - 1}{\ln r_i^q} & \Leftrightarrow q \neq 0, a = 0 \\ \frac{\ln r_i^q}{r_i^q - 1} & \Leftrightarrow q \neq 0, a \neq 0, a = -q \\ \frac{a}{a+q} \frac{1-r_i^{a+q}}{1-r_i^a} & \Leftrightarrow q \neq 0, a \neq 0, a \neq -q \end{cases} \quad (10)$$

Finally, from Eq. (9) one obtains

$$m = \frac{S_\nu}{\frac{2k\nu^2}{c^2} T_0} \frac{1}{F} \quad (11)$$

or, equivalently,

$$M = \frac{S_\nu d^2 \mathcal{R}}{\kappa(\nu) \frac{2k\nu^2}{c^2} T_0} \frac{1}{F} \quad (12)$$

which is analogous to Eq. (1) when the temperature and density gradients are taken into account. We stress that these equations are valid only in the optically thin limit and under the RJ approximation.

It is interesting to discuss the transition between optically thin and optically thick regimes. The critical value of m for which such a transition occurs is obtained by equating the flux density from Eq. (4), in the RJ limit, to that from Eq. (9):

$$m_c = \frac{\Omega_0}{F}. \quad (13)$$

We note that the (approximate) relationship between S_ν and m is fully determined by Eqs. (4) and (13), because once the optically thick flux and the critical value of m are fixed, also the optically thin flux is univocally established. This fact can be used to study the dependence of S_ν on the various physical parameters.

The behaviour of S_ν as a function of m is illustrated by the dashed curves in Fig. 1. In all panels the green curve corresponds to the approximate expressions of S_ν for a set of parameters arbitrarily chosen for illustrative purposes. These are $\nu = 220 \text{ GHz}$, $\theta_0 = R_0/d = 1''$, $r_i = 0.01$, $T_0 = 50 \text{ K}$, $q = -0.4$, $p = -1.5$ (i.e. $a = 1.5$). The blue and red curves are obtained by varying only one of these parameters, as detailed in each panel.

In particular, we observe that both the optically thick flux from Eq. (4) and m_c are proportional to Ω_0 , but only the former depends on T_0 . This implies that for increasing T_0 the flux density increases, while the transition between the thin and thick regimes occurs approximately¹ at the same value of m . Instead, for increasing Ω_0 both the thick flux and m_c increase by the same factor, while the optically thin flux remains the same (because Eq. (9) does not depend on R_0). Finally, it can be shown that function F is increasing with r_i if $q > 0$ and decreasing if $q < 0$ (see Appendix A), which in turn implies that a variation of r_i affects only m_c and not the optically thick flux density.

The solid curves in the figure represent the flux density computed with the numerical model described in the next section, which properly takes into account the dust optical depth and does not assume the RJ approximation.

¹ The slight shift of m_c of the red curve in the bottom panel of Fig. 1 is due to the RJ approximation being unsuited for $T_0 = 10 \text{ K}$ and $\nu = 220 \text{ GHz}$.

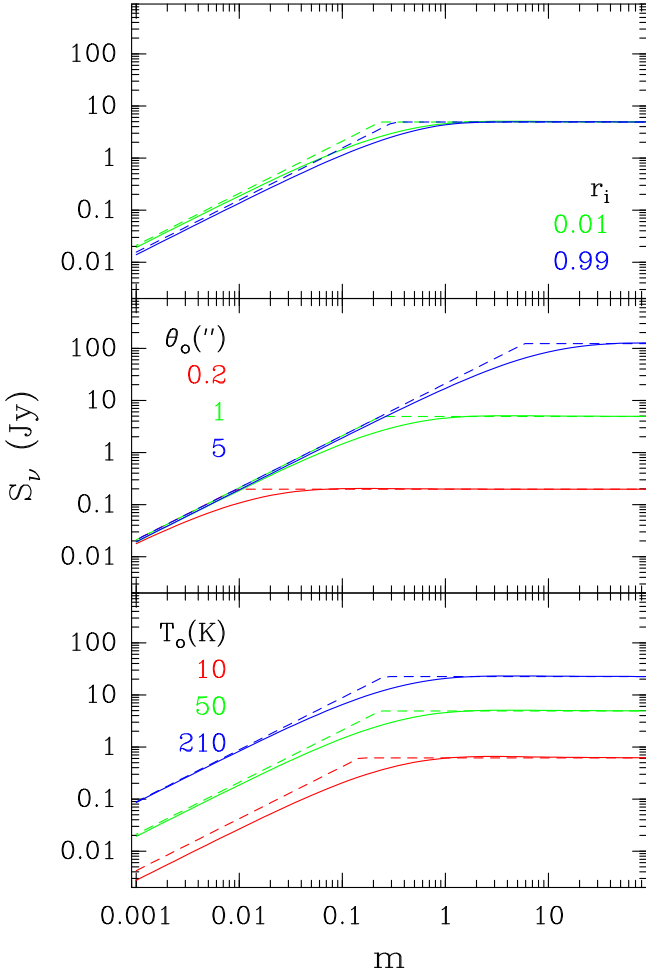


Fig. 1. Template flux densities from a spherical dusty clump as a function of parameter m (see text). The curves are obtained for illustrative purposes from fiducial values of the input parameters, i.e. $\nu = 220$ GHz, $\theta_o = R_o/d = 1''$, $r_i = 0.01$, $T_o = 50$ K, $q = -0.4$, $p = -1.5$. In each panel only one of these parameters is changed as indicated in the panel itself. Dashed curves represent the approximate analytical solutions given by Eq. (9), while solid curves are obtained from the numerical model described in Sect. 2.2.

2.2. Numerical solution

It is possible to obtain an exact semi-analytical expression of S_ν as a function of the clump mass only in the simple case $q = 0$ and $p = 0$. The result is given by Eq. (A.4) of Cesaroni et al. (2019), which with our notation takes the form

$$S_\nu = \Omega_o B_\nu(T) \times \left[1 + \frac{2}{\tau_o} \left(\sqrt{1-r_i^2} e^{-\tau_o} \sqrt{1-r_i^2} + \frac{e^{-\tau_o} \sqrt{1-r_i^2} - 1}{\tau_o} \right) - \int_0^{r_i^2} e^{-\tau_o(\sqrt{1-t} - \sqrt{r_i^2-t})} dt \right] \quad (14)$$

where $\tau_o = 2R_o \kappa \rho_o = 3m/(2\Omega_o)$.

More in general, the clump flux density can be estimated numerically as the integral of the brightness I_ν over the source solid angle, namely

$$S_\nu = \int_{\Omega_o} I_\nu d\Omega = \frac{1}{d^2} \int_0^{R_o} I_\nu(x) 2\pi x dx = 2\Omega_o \int_0^1 I_\nu(\xi) \xi d\xi \quad (15)$$

where x is the projected radius on the plane of the sky and we assume $\xi = x/R_o$.

It is convenient to split the calculation of the brightness along an arbitrary l.o.s. through the clump into two parts, for positive and negative values of z , as follows:

$$I_\nu^0 = I_\nu^{\text{BG}} e^{-\int_{z_m}^{\infty} \kappa \rho dz} + \int_{z_m}^{\infty} B_\nu e^{-\int_{z_m}^z \kappa \rho dz'} \kappa \rho dz \quad (16)$$

$$I_\nu = I_\nu^0 e^{-\int_{-z_m}^{\infty} \kappa \rho dz} + \int_{-z_m}^{\infty} B_\nu e^{-\int_{-z_m}^z \kappa \rho dz'} \kappa \rho dz \quad (17)$$

where z is the Cartesian coordinate along the line of sight (l.o.s.), I_ν^{BG} is the background brightness, the observer is located at $z = -\infty$, and we define

$$z_M = \sqrt{R_o^2 - x^2} \quad (18)$$

$$z_m = \begin{cases} \sqrt{r_i^2 - x^2} & \Leftrightarrow 0 \leq x < r_i \\ 0 & \Leftrightarrow r_i \leq x \leq R_o \end{cases} \quad (19)$$

(see Figs. 2a and 2b for a sketch of two representative l.o.s.).

In the following we focus on the solution of Eq. (16). The emergent brightness at $z = -z_M$ given by Eq. (17) can be calculated with the same approach described below, once I_ν^0 has been computed.

In order to obtain an approximate analytical solution of Eq. (16), we divide the part of the clump which contributes to the radiation along the given l.o.s. into a suitable number of shells, N_S , and assume that in each shell the relevant physical parameters (density and temperature) are constant. Figure 2a shows a sketch of the shells for a generic l.o.s. with $x > R_i$, where only the dust between $R = x$ and $R = R_o$ contributes to the brightness, while Fig. 2b refers to the l.o.s. with $0 \leq x < R_i$, where the portion contributing to I_ν is the whole shell between $R = R_i$ and $R = R_o$.

Under the previous approximation, Eq. (16) takes the form

$$I_\nu^0 = I_\nu^{\text{BG}} e^{-\sum_{j=1}^{N_S} \int_{z_{j-1}}^{z_j} \kappa \rho dz} + \sum_{j=1}^{N_S} \int_{z_{j-1}}^{z_j} B_\nu(T) e^{-\int_{z_m}^{z_{j-1}} \kappa \rho dz' - \int_{z_{j-1}}^z \kappa \rho dz'} \kappa \rho dz \simeq I_\nu^{\text{BG}} e^{-\sum_{j=1}^{N_S} \kappa \rho_j (z_j - z_{j-1})} + \sum_{j=1}^{N_S} B_\nu(T_j) e^{-\sum_{l=1}^{j-1} \kappa \rho_l (z_l - z_{l-1})} \kappa \rho_j \int_{z_{j-1}}^{z_j} e^{-\kappa \rho_j (z - z_{j-1})} dz = I_\nu^{\text{BG}} e^{-\sum_{j=1}^{N_S} \tau_j} + \sum_{j=1}^{N_S} B_\nu(T_j) (1 - e^{-\tau_j}) e^{-\sum_{l=1}^{j-1} \tau_l} \quad (20)$$

where we define $z_0 = z_m$, $\sum_{l=1}^0 \tau_l = 0$, $\tau_j = \kappa \rho_j (z_j - z_{j-1})$, $T_j = T(R_j)$, and $\rho_j = \rho(R_j)$, with R_j outer radius of shell j . The opacity of shell j can be written as

$$\tau_j = \kappa \rho_o R_o r_j^p \left(\sqrt{r_j^2 - \xi^2} - \sqrt{r_{j-1}^2 - \xi^2} \right) = \frac{m}{4\Omega_o} \frac{r_j^{a-3}}{\int_{r_i}^1 r^{a-1} dr} \left(\sqrt{r_j^2 - \xi^2} - \sqrt{r_{j-1}^2 - \xi^2} \right) \quad (21)$$

where we used Eq. (8).

Equation (20) can be easily implemented in a computer code as it is equivalent to iteratively solving the radiative transfer

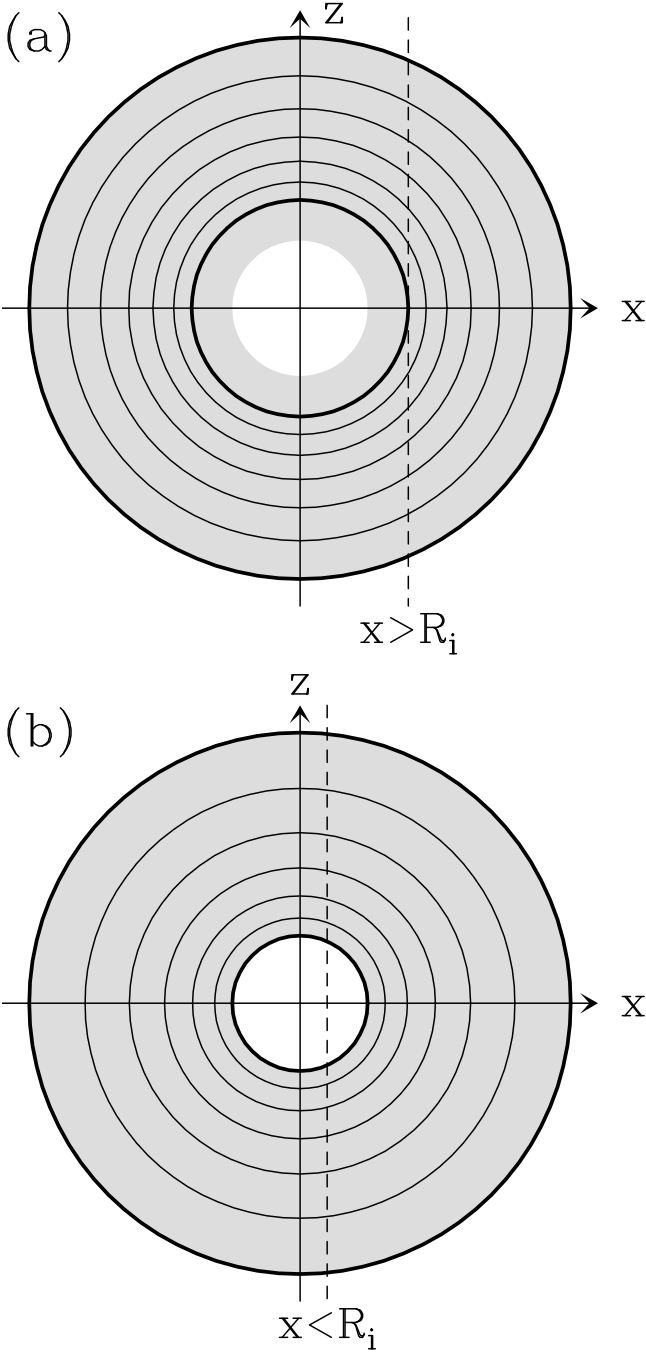


Fig. 2. Sketch of two lines of sight (dashed lines) through a spherically symmetric clump (grey area) with impact parameter x , crossing (bottom panel) and not crossing (top panel) the central cavity of radius R_i (white central area). The thick circles denote the minimum and maximum radius of the region contributing to the brightness along the given l.o.s., while the thin circles are template annuli defined by Eq. (27), to be used for the numerical integration of the radiative transfer equation.

equation for each shell, using as input the output brightness of the previous shell crossed by the l.o.s..

The major problem with this approach is that a priori both the density and/or temperature laws may be very steep close to the clump center, if q and/or p are negative. Therefore, the thickness of the shells cannot be constant and must be adapted to the local value of the density and temperature gradients. We propose a simple way to get around this problem.

In practice, what matters for our purposes is to estimate the flux density to a desired level of accuracy, δS_ν . This means that we should divide the clump into a number of shells, N_S , such that each of them does not contribute more than δS_ν to the total flux density. For a given l.o.s. with impact parameter x , the shells to be considered in Eq. (20) are those with $R \geq x$, if $x > R_i$, and $R \geq R_i$, if $x \leq R_i$ (see Fig. 2). Thus the total flux density of interest for the integration along the given l.o.s. is that emitted between $r = r_0 = \max\{x, R_i\}$ and $r = 1$. This implies that a suitable value of N_S is given by

$$N_S = \left\lceil \frac{S_\nu(r_0; 1)}{\delta S_\nu} \right\rceil + 1. \quad (22)$$

Here the square brackets indicate the integer part of the argument and 1 is added to prevent the case $N_S = 0$. Moreover, we use the notation $S_\nu(r_1; r_2)$ to indicate the flux density emitted between two generic radii $R_1 < R_2$, which implies that $S_\nu(r_1; 1)$ is the total flux density emitted by the clump.

The expression for the radius of a generic shell, j , is derived by imposing that each shell equally contributes with a fraction $1/N_S$ to the total flux density $S_\nu(r_0; 1)$, namely

$$S_\nu(r_{j-1}; r_j) = \frac{S_\nu(r_0; 1)}{N_S} \quad (23)$$

for any $j = 1, \dots, N_S$, under the assumption that $r_j > r_{j-1}$.

An approximate expression of $S_\nu(r_1; r_2)$, with $r_1 < r_2$, can be calculated in the optically thin and RJ limits from Eq. (7):

$$S_\nu(r_1; r_2) \propto \int_{r_1}^{r_2} r^{a+q-1} dr = \begin{cases} \frac{r_2^{a+q} - r_1^{a+q}}{a+q} & \Leftrightarrow a+q \neq 0 \\ \ln\left(\frac{r_2}{r_1}\right) & \Leftrightarrow a+q = 0 \end{cases} \quad (24)$$

Substituting this expression in Eq. (23), one obtains

$$r_j^{a+q} = r_{j-1}^{a+q} + \frac{1 - r_0^{a+q}}{N_S} \quad (25)$$

for $a+q \neq 0$, and

$$\ln r_j = \ln r_{j-1} - \frac{\ln r_0}{N_S} \quad (26)$$

for $a+q = 0$. Since these expressions hold for any j , after some algebra one can finally write

$$r_j = \begin{cases} \left(r_0^{a+q} + j \frac{1 - r_0^{a+q}}{N_S} \right)^{\frac{1}{a+q}} & \Leftrightarrow a+q \neq 0 \\ r_0^{1 - \frac{j}{N_S}} & \Leftrightarrow a+q = 0. \end{cases} \quad (27)$$

Using Eq. (24) and setting $\delta S_\nu = \varepsilon S_\nu(r_i; 1)$, one can also conveniently re-write Eq. (22) as

$$N_S = \left\lceil \frac{S_\nu(r_0; 1)}{\varepsilon S_\nu(r_i; 1)} \right\rceil + 1 = \left\lceil \frac{1 - r_0^{a+q}}{\varepsilon (1 - r_i^{a+q})} \right\rceil + 1 \quad (28)$$

where ε is the fraction of the total flux density emitted by the clump that we want to be contributed by each shell.

The solid curves in Fig. 1 are the numerical solutions obtained for the same set of parameters as the dashed curves with the same colour. For the sake of simplicity, in our calculations we have assumed $I_\nu^{\text{BG}} = 0$. While, as expected, the numerical solution tends to converge to the corresponding approximate analytical solution for large and small values of m , the two may differ significantly for intermediate values of m . Moreover, some difference is also seen at small values of m due to the RJ approximation. In Sect. 2.3 we discuss all these features in more detail.

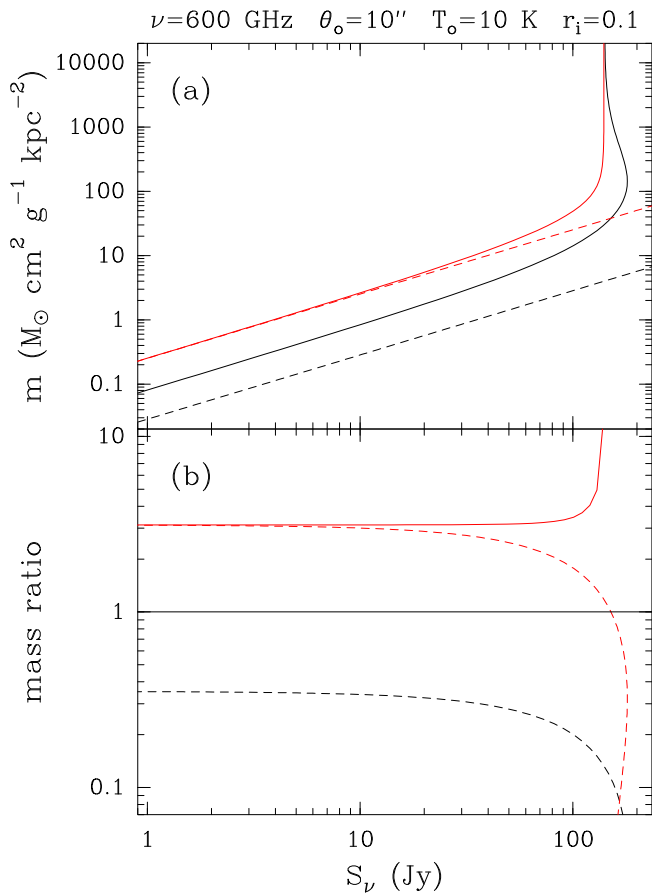


Fig. 3. *Panel a:* Plot of m versus the total flux density of the clump. The red curves correspond to the case $q = 0$ and $p = 0$, while the black curves are for models allowing for temperature and density gradients. The dashed black curve has been obtained under the optically thin and RJ approximations from Eq. (11), whereas the dashed red curve is computed in the optically thin limit from Eq. (1). *Panel b:* Mass ratios between all the curves in the top panel and the black solid curve.

2.3. Limits of the approximate analytical solutions

The main goal of our study is to establish how much the conversion from flux to mass can be affected by the usual assumption of constant dust density and temperature. Therefore, it is convenient to consider the inverse relationship with respect to those in Fig. 1 and plot the core mass as a function of the flux density. With this in mind, in Fig. 3a we show a plot of m , our proxy for the clump mass, versus S_{ν} . For illustrative purposes, we have considered an extreme case with $\nu = 600$ GHz, $\theta_0 = 10''$, $T_0 = 10$ K, $q = -0.5$, $p = -2$, and $r_i = 0.1$, which emphasizes the drawbacks of using an approximate solution, as we show later. This set of parameters could represent a typical clump observed e.g. in the Hi-GAL survey at $500 \mu\text{m}$.

For the sake of comparison, in the same figure beside the numerical solution (black solid curve) we plot also the approximate analytical solution in the optically thin and RJ limits (black dashed curve) from Eq. (9), and the relationships (red curves) obtained under the commonly used assumption of constant density and temperature (equal to ρ_0 and T_0 , respectively). In particular, the red solid curve corresponds to the solution from Eq. (14) while the red dashed curve is computed in the optically thin limit from Eq. (1).

To emphasize the comparison between the various curves, in Fig. 3b we plot the ratio between the masses derived un-

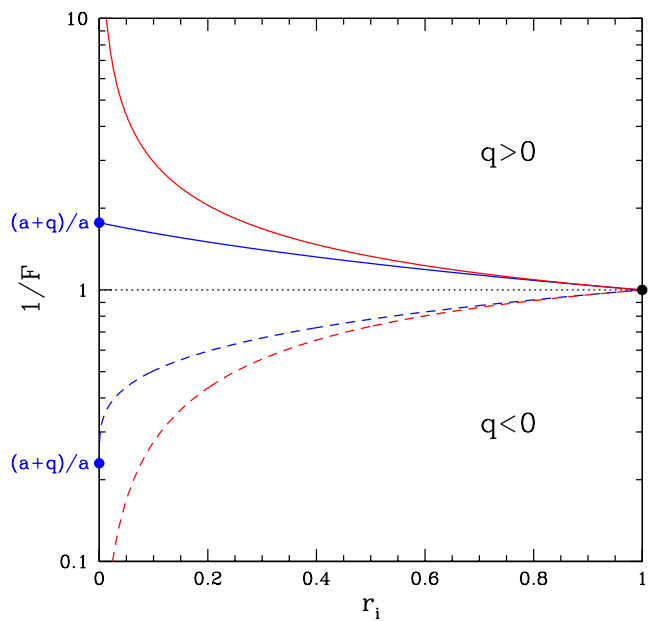


Fig. 4. Plot of $1/F$ as a function of r_i . Besides the trivial case $q = 0$ (dotted line), four representative cases have been considered. Dashed and solid lines correspond, respectively, to $q < 0$ and $q > 0$, while blue indicates curves with $a + q > 0$ and $a > 0$ and red all the other cases. The blue dots mark the value $((a + q)/a)$ of the corresponding curve for $r_i \rightarrow 0^+$ and the black dot indicates the limit (1) of all curves for $r_i \rightarrow 1^-$.

der the different approximations and that computed numerically. Clearly, at low fluxes the optically thin approximation is valid, as demonstrated by the excellent match between the solid and dashed red curves. However, for the same fluxes one sees a significant difference between the solid and dashed black curves, due to the RJ approximation. At high fluxes the deviation with respect to the numerical solution is very prominent until the emission saturates due to the large opacity and a mass estimate cannot be obtained because of degeneracy of the solution.

We remark that the above example is proposed only for illustrative purposes. More in general, one must keep in mind that the deviation from the correct solution is sensitive to the input parameters of the model. This is especially true for the observing frequency and dust temperature, on which the goodness of the RJ approximation depends, and the steepness of the temperature and density gradients. The effect of such gradients can be seen by taking the ratio in the optically thin and RJ limits between the mass from Eq. (12) and that from Eq. (1). It is straightforward to demonstrate that such a ratio is equal to $1/F$, which depends only on r_i , q , and p or, equivalently, a . This result relies upon the assumption that the temperature used in Eq. (1) is T_0 . In fact, most studies derive the clump temperature from a modified black-body fit to the SED of the source, which usually peaks in the far-IR, where the emission is optically thick and traces the outer layers of the clump. Therefore, the temperature thus derived is very close to T_0 .

Figure 4 shows the typical behaviour of $1/F$ as a function of r_i (see also Appendix A), for $q = 0$ (dotted line), $q \neq 0$, $a \neq 0$, $a + q \neq 0$ (blue curves), and in all the other cases (red curves). One sees that a priori the presence of temperature and density gradients may lead to largely underestimate (if $q > 0$) or overestimate (if $q < 0$) the mass of the clump, for sufficiently small values of r_i . Whether this occurs in practice and to what extent is discussed by means of a few examples in Sect. 4.

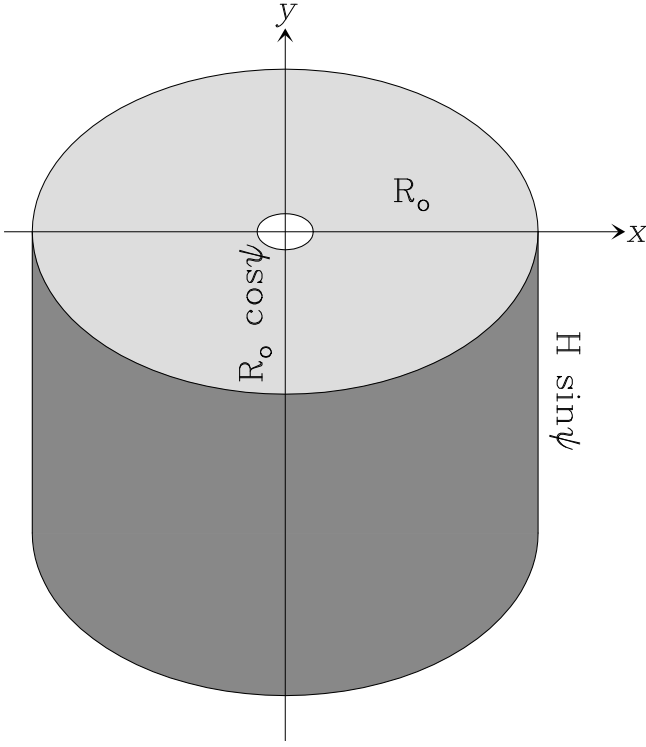


Fig. 5. Sketch of a cylindrical clump seen with an inclination angle ψ between the symmetry axis and the l.o.s.. The figure represents the projection of the cylinder on the plane of the sky, where the Cartesian system x, y lies. The radius and height of the cylinder are, respectively, R_o and H .

3. Flux density of cylindrical clump

Now, we compute the total flux density emerging from a cylindrically symmetric clump with height H , inner radius R_i , and outer radius R_o . This model might be more appropriate, e.g., for (part of) those filamentary structures observed all over the Galaxy. Figure 5 shows the projection of the clump over the plane of the sky for a generic inclination angle, ψ , between the l.o.s. and the symmetry axis ($\psi = 0$ corresponds to face on). Temperature and density depend only on R through Eqs. (2) and (3).

3.1. Approximate analytical expression

As already done in Sect. 2, it is instructive as a first step to consider the solution in the optically thin and thick limits.

3.1.1. Optically thick case

If the opacity is large, the flux is obtained by integrating the surface brightness over the solid angle subtended by the source. This is the sum of the integral over the light-grey and the dark-grey areas in Fig. 5. The latter has constant brightness equal to $B_v(T_o)$ and surface comprised between two half ellipses described by the expressions

$$y_1 = \cos \psi \sqrt{R_o^2 - x^2} - H \sin \psi \quad (29)$$

$$y_2 = \cos \psi \sqrt{R_o^2 - x^2} \quad (30)$$

where x and y are Cartesian coordinates lying in the plane of the sky and oriented as shown in Fig. 5. The flux density of such a

surface is hence given by

$$S_v^A = \frac{B_v(T_o)}{d^2} \int_{-R_o}^{R_o} dx \int_{y_1(x)}^{y_2(x)} dy = \frac{2R_o H}{d^2} B_v(T_o) \sin \psi. \quad (31)$$

The brightness over the light-grey ellipse in Fig. 5 varies with R and the corresponding flux density is computed as follows:

$$\begin{aligned} S_v^B &= \frac{4}{d^2} \left[\int_0^{R_i} dx \int_{y_i(x)}^{y_o(x)} B_v dy + \int_{R_i}^{R_o} dx \int_0^{y_o(x)} B_v dy \right] \\ &= \frac{4 \cos \psi}{d^2} \left[\int_0^{R_i} dX \int_{Y_i(X)}^{Y_o(X)} B_v(T(R)) dY \right. \\ &\quad \left. + \int_{R_i}^{R_o} dX \int_0^{Y_o(X)} B_v(T(R)) dY \right] \end{aligned} \quad (32)$$

where $Y_i = \sqrt{R_i^2 - x^2}$, $Y_o = \sqrt{R_o^2 - x^2}$, $y_i = Y_i \cos \psi$, and $y_o = Y_o \cos \psi$, with X, Y Cartesian coordinates perpendicular to the cylinder axis, related to the x, y system through the expressions $x = X$, $y = Y \cos \psi$. In practice, Eq. (32) is the integral of B_v over the face of the cylinder, multiplied by $\cos \psi$. This integral is more conveniently expressed in polar coordinates as

$$\begin{aligned} S_v^B &= \frac{4 \cos \psi}{d^2} \int_0^{\frac{\pi}{2}} d\phi \int_{R_i}^{R_o} B_v(T(R)) R dR \\ &= 2 \cos \psi \frac{\pi R_o^2}{d^2} \int_{r_i}^1 B_v(T(r)) r dr \end{aligned} \quad (33)$$

The total flux density is hence given by the sum $S_v^A + S_v^B$, namely

$$S_v = \Omega_o^e \sin \psi B_v(T_o) + 2 \Omega_o \cos \psi \int_{r_i}^1 B_v(T(r)) r dr \quad (34)$$

where $\Omega_o^e = 2R_o H/d^2$ is the solid angle subtended by the clump seen edge on. In the RJ approximation one obtains

$$S_v \simeq \frac{2k\nu^2}{c^2} T_o \left(\Omega_o^e \sin \psi + 2 \Omega_o \cos \psi \int_{r_i}^1 r^{q+1} dr \right) \quad (35)$$

with

$$\int_{r_i}^1 r^{q+1} dr = \begin{cases} \frac{1-r_i^{q+2}}{q+2} & \Leftrightarrow q \neq -2 \\ -\ln r_i & \Leftrightarrow q = -2. \end{cases} \quad (36)$$

3.1.2. Optically thin case

In the optically thin limit, the flux density does not depend on the inclination angle because by definition the observer sees all the particles of the clump that contribute to the photon budget, independently of the shape and orientation of the clump. Therefore, the source luminosity is computed by integrating the emissivity over the clump volume:

$$S_v = \frac{H}{4\pi d^2} \int_{R_i}^{R_o} 4\pi \kappa \rho(R) B_v(T(R)) 2\pi R dR \quad (37)$$

$$\simeq 2 \frac{\pi R_o^2 H}{d^2} \rho_o \kappa \frac{2k\nu^2}{c^2} T_o \int_{r_i}^1 r^{p+1} dr. \quad (38)$$

where we have adopted the RJ approximation. Since the mass of the clump is equal to

$$M = \int_{R_i}^{R_o} \rho(R) \mathcal{R} 2\pi R H dR = 2\pi H R_o^2 \rho_o \mathcal{R} \int_{r_i}^1 r^{p+1} dr \quad (39)$$

one finally obtains

$$S_\nu = \frac{\kappa M}{\mathcal{R} d^2} \frac{2k\nu^2}{c^2} T_o \frac{\int_{r_i}^1 r^{q+p+1} dr}{\int_{r_i}^1 r^{p+1} dr} = m \frac{2k\nu^2}{c^2} T_o F(r_i; q, a). \quad (40)$$

This expression is formally identical to Eq. (9), with the only difference that this time we have defined $a = p + 2$.

3.2. Numerical solution

Now, we consider the general case with moderate opacity, which allows only a numerical solution. The calculation of the flux density for an arbitrary inclination angle is quite complicated and goes beyond the scope of the present study. Here, we consider only the two extreme inclinations: face-on and edge-on.

3.2.1. Edge-on cylindrical clump

The calculation of S_ν is formally identical to that developed in Sect. 2.2, with the only difference that Eq. (15) must be replaced with

$$S_\nu = \int_{\Omega_s^e} I_\nu d\Omega = \frac{2}{d^2} \int_0^{R_o} I_\nu(x) H dx = \Omega_o^e \int_0^1 I_\nu(\xi) \xi d\xi. \quad (41)$$

The brightness I_ν can be obtained by integrating along the l.o.s. exactly as described in Sect. 2.2, provided $a = p + 3$ is replaced with $a = p + 2$.

3.2.2. Face-on cylindrical clump

If the l.o.s. is parallel to the axis of the cylindrical clump, the flux density is computed from Eq. (15). The expression of the brightness, I_ν , is easily obtained because for a given x the density and temperature are constant along the l.o.s., hence

$$I_\nu(\xi) = I_\nu^{\text{BG}} e^{-H\kappa\rho_o\xi^p} + B_\nu(T_o \xi^q) (1 - e^{-H\kappa\rho_o\xi^p}) \quad (42)$$

where we remind the reader that we have defined $\xi = x/R_o$.

4. Application to practical cases

As a test bed for the clump model previously described, we consider three examples taken from the literature. In two of these, the mass was estimated under the usual hypothesis of constant temperature and density and assuming optically thin emission.

4.1. The hot molecular core G31.41+0.31

As a first example, we consider the hot molecular core (HMC) G31.41+0.31, for which Beltrán et al. (2018; hereafter BEL18) derived a mass estimate from the 1.4 mm continuum emission imaged with ALMA. This case is especially suitable for our purposes because these authors obtained also an estimate of the temperature and density profiles as a function of the HMC radius. We adopt the same parameters used in their calculation, namely $d = 7.9$ kpc, $R_o = 1''.076$, $q = -0.77$, $p = -2$, $\kappa(217\text{GHz}) = 0.8$, and $\mathcal{R} = 100$. The total flux density of the core at $\nu = 217$ GHz is $S_\nu = 3.1$ Jy. The only unknown parameter is r_i , which BEL18 implicitly assumed equal to 0. In Fig. 6 we plot the values of the mass estimated in different ways, as a function of r_i .

The mass obtained from our numerical solution (i.e. without any approximation) is represented by the black solid curve, while

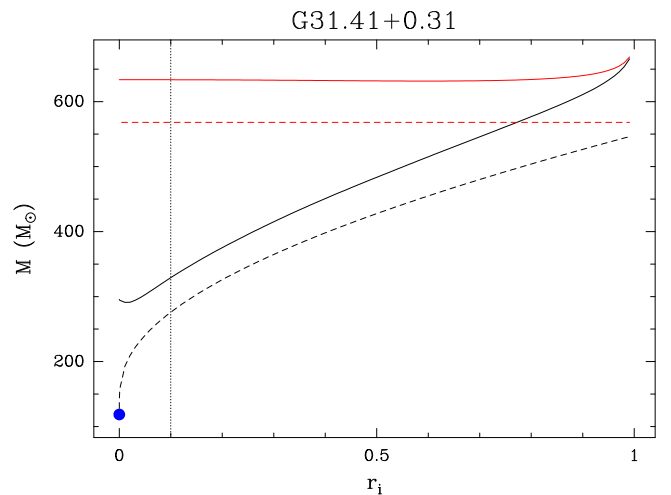


Fig. 6. Mass of the HMC G31.41+0.31 as a function of r_i . The input parameters are $d = 7.9$ kpc, $R_o = 1''.076$, $q = -0.77$, $p = -2$, $\kappa(217\text{GHz}) = 0.8$, $\mathcal{R} = 100$, $S_{217\text{GHz}} = 3.1$ Jy. The black lines are for $q = -0.77$ and $p = -2$, whereas the red lines correspond to $q = 0$ and $p = 0$. Both dashed lines are obtained in the optically thin limit, while the black dashed line assumes also the RJ approximation. The blue dot corresponds to the value of the mass computed by BEL18. The dotted vertical line marks a plausible upper limit for r_i (see text).

that derived under the optically thin and RJ approximations is shown as a dashed black curve. For the sake of comparison, we also mark with a blue dot the mass computed from Eq. (6) of BEL18. The resulting expression differs from our Eq. (12) by only a factor $(2/\sqrt{\pi})[\Gamma(-(p+q)/2)/\Gamma(-(p+q+1)/2)] \simeq 0.927$. The latter is due to the fact that BEL18 calculated the brightness by integrating along the line of sight from $-\infty$ to $+\infty$, whereas we limit our integration to the sphere of radius R_o . Finally, we report in the same figure also the mass estimated from Eq. (14) (i.e. without the RJ approximation and assuming constant temperature and density) both with (red dashed curve) and without (red solid curve) the optically thin assumption.

The largest difference between the various curves occurs for $r_i = 0$, not surprisingly because at small radii the effect of the temperature gradient is enhanced. Vice versa, for r_i close to 1, the temperature variation across the core is minimum and all curves converge towards the $q = 0$ solution corresponding to the red curves. In particular, the BEL18 solution for $r_i = 0$ is smaller than our numerical solution by a factor ~ 2 , whereas the constant-temperature solutions predict a mass in excess by at least a factor ~ 2 . It is also worth noting that the emission is partially thick in this HMC, as proved by the gap between the solid curves and the corresponding dashed curves.

The assumption $r_i = 0$ is obviously unrealistic, as the temperature and density laws must break down at some point close to the HMC center. A plausible hypothesis is that R_i is comparable to half the separation ($0''.1$) between the two free-free sources detected by Cesaroni et al. (2010) close to the core center, which implies $r_i \simeq 0.1$ (see dotted line in Fig. 6). For this value the discrepancy among the different estimates of the mass is less prominent, but may still amount to 70%, which might not be negligible when comparing the core mass to other parameters such as the virial mass or the magnetic critical mass.

4.2. Stability of massive star-forming clumps

Another convenient test-case for our model is represented by the sample of massive clumps observed by Fontani et al. (2002; hereafter FON02). In fact, also in this case as for BEL18 a direct estimate of the temperature and density gradients was obtained by the authors, who find $q = -0.54$ and $p = -2.6$. A puzzling result of their study is that the ratio between the clump masses and the corresponding virial masses is >1 (see their Fig. 6), which hints at some additional support to stabilize the clumps, such as e.g. magnetic fields. However, the mass estimates made by FON02 were derived without taking into account the temperature and density gradients inside the clumps. Here, we want to reconsider the problem by applying the appropriate corrections for these gradients.

At the time of FON02 no homogeneous data set was available for the continuum emission of the clumps at (sub)mm wavelengths, and the authors had to rely upon a miscellany of observations obtained with various telescopes. Now, the situation has changed and we can take advantage of Galaxy-wide surveys such as the APEX Telescope Large Area Survey of the Galaxy (ATLASGAL; Schuller et al. 2009), which covers almost all of the clumps studied by FON02.

We recalculated the clump masses using the flux densities at $\nu = 345$ GHz from the ATLASGAL compact source catalogue (Urquhart et al. 2014; hereafter URQ14). For the sake of consistency with FON02, we adopt their distances, whereas we take the clump angular radius from URQ14 and T_o from Urquhart et al. (2018; hereafter URQ18). The latter is obtained from a modified black-body fit to the SED and is hence a good approximation of the temperature at the surface of the clump, because the SEDs of these objects typically peak around $\sim 100 \mu\text{m}$ where the emission is optically thick. We also adopt $\kappa = 1.85 \text{ cm}^2 \text{ g}^{-1}$ and $\mathcal{R} = 100$ as in Schuller et al. (2009), and assume $r_i = 0.01$ based on the fact that the density gradient with $p = -2.6$ appears to hold on a range of radii spanning two orders of magnitude (see Fig. 10 of FON02).

The virial masses, M_{vir} , have been recalculated, using the line widths, ΔV , from FON02 and the new values of R_o and T_o from URQ14 and URQ18. In our estimates, unlike FON02, we take into account the correction to M_{vir} due to the density and temperature profiles, as detailed in Appendix B.

Figure 7 is the same as Fig. 6 of FON02 and shows the ratio between the clump mass and the corresponding virial mass for the different sources. We have also evaluated a mean error on this ratio taking into account that to a good approximation $M_{\text{clump}}/M_{\text{vir}} \propto S_\nu/[T_o(\Delta V)^2 \theta_o]$ and assuming an uncertainty of 20% for all variables. The plot confirms that basically all clump masses are significantly greater than the corresponding virial masses (black circles), if the clump mass is estimated with constant temperature and density. However, when the temperature and density gradients are taken into account with our numerical model, almost all clumps become virialized (red squares). This result proves that the correction applied may be crucial for stability issues.

4.3. Masses of the ATLASGAL compact sources

As a last example, we discuss how temperature and density gradients could affect the estimates of the masses of the clumps identified in the ATLASGAL compact source catalogue by URQ18. In particular, we calculate the ratio between the mass computed with our method and that obtained by URQ18 from Eq. (1). For our estimates, θ_o and S_ν were taken from Table 1

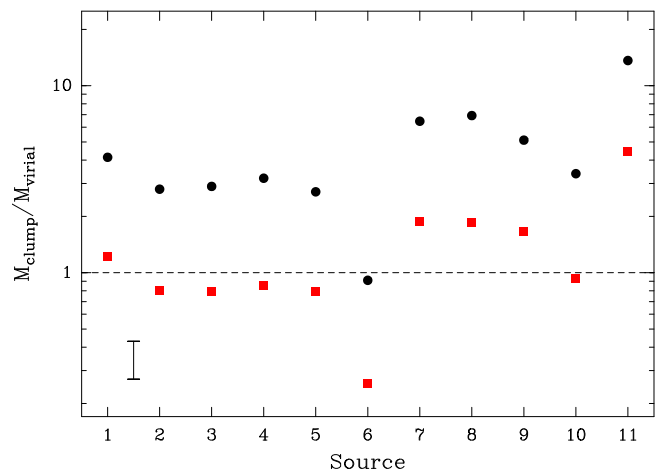


Fig. 7. Same as Fig. 6 of FON02, where the clump masses have been recomputed with our numerical solution using the temperature, radii, and flux densities from the ATLASGAL compact source catalogue, and the virial masses have been corrected to take into account density and temperature gradients. The numbers on the x-axis identify the clumps according to the numbering of Table 1 of FON02. Black circles correspond to constant density and temperature, as assumed by FON02, whereas red squares are obtained adopting $q = -0.54$ and $p = -2.6$, consistent with the findings of FON02. The error bar in the bottom left indicates the typical uncertainty on the mass ratio.

of URQ14, T_o and d from Table 5 of URQ18, and we assume $\kappa(345 \text{ GHz}) = 1.85 \text{ cm}^2 \text{ g}^{-1}$ and $\mathcal{R} = 100$ for consistency with URQ18. We also set $r_i = 0.01$ for the reason explained in Sect. 4.2.

In Fig. 8 we plot the ratio between our numerical mass estimate, obtained as described in Sect. 2.2, and the mass computed by URQ18 (black dots), as a function of the latter (M_o^{thin}). The calculation is made for the fiducial values of $q = -0.4$, $p = -1.5$ (top panel) and for $q = -0.54$, $p = -2.6$ in the footsteps of Sect. 4.2 (bottom panel). The mean ratio is, respectively, 0.64 and 0.25, which represent a non-negligible correction for estimates of quantities such as e.g. the virial parameter.

It is instructive to examine the separate contributions of opacity, RJ approximation, and temperature and density gradients to the correction factor. This can be done by trivially rewriting the mass ratio as

$$\frac{M}{M_o^{\text{thin}}} = \left(\frac{M}{M^{\text{RJ}}} \frac{M_o^{\text{RJ-thin}}}{M_o^{\text{thin}}} \right) \frac{M^{\text{RJ}}}{M_o^{\text{RJ-thin}}} \frac{M_o^{\text{RJ-thin}}}{M_o^{\text{thin}}} \quad (43)$$

where the indices ‘‘RJ’’ and ‘‘thin’’ indicate, respectively, that the mass is calculated in the RJ and in the optically thin approximation, while the subscript ‘‘o’’ means that the calculation is done for constant temperature and density (i.e. $T = T_o$ and $\rho = \rho_o$).

In the right-hand side of Eq. (43), the term in parentheses is sensitive to the RJ approximation, the ratio $M^{\text{RJ}}/M_o^{\text{RJ-thin}}$ is related to the opacity of the clump, and $M_o^{\text{RJ-thin}}/M_o^{\text{thin}} = 1/F$ is the correction for the temperature and density gradients. These three quantities are plotted in Fig. 8 as red dots ($M^{\text{RJ}}/M_o^{\text{RJ-thin}}$), blue dots ($MM_o^{\text{RJ-thin}}/(M^{\text{RJ}} M_o^{\text{thin}})$), and a green line ($M_o^{\text{RJ-thin}}/M_o^{\text{thin}}$).

We conclude that the most important correction is due to the gradients, although in a non-negligible number of clumps opacity may play an important role, provided the temperature and density gradients are sufficiently steep.

Table 1. Approximate expressions of the flux density of a clump with density and temperature gradients, in the RJ limit (for the definition of the symbols, see Sects. 2 and 3)

opacity	S_ν spherical symmetry	S_ν cylindrical symmetry
$\tau \ll 1$	$\frac{\kappa M}{Rd^2} \frac{2k\nu^2}{c^2} T_0 F(r_i; q, p + 3)$	$\frac{\kappa M}{Rd^2} \frac{2k\nu^2}{c^2} T_0 F(r_i; q, p + 2)$
$\tau \gg 1$	$\Omega_0 \frac{2k\nu^2}{c^2} T_0$	$\frac{2k\nu^2}{c^2} T_0 \left(\Omega_0^e \sin \psi + 2 \Omega_0 \cos \psi \int_{r_i}^1 r^{-q+1} dr \right)$

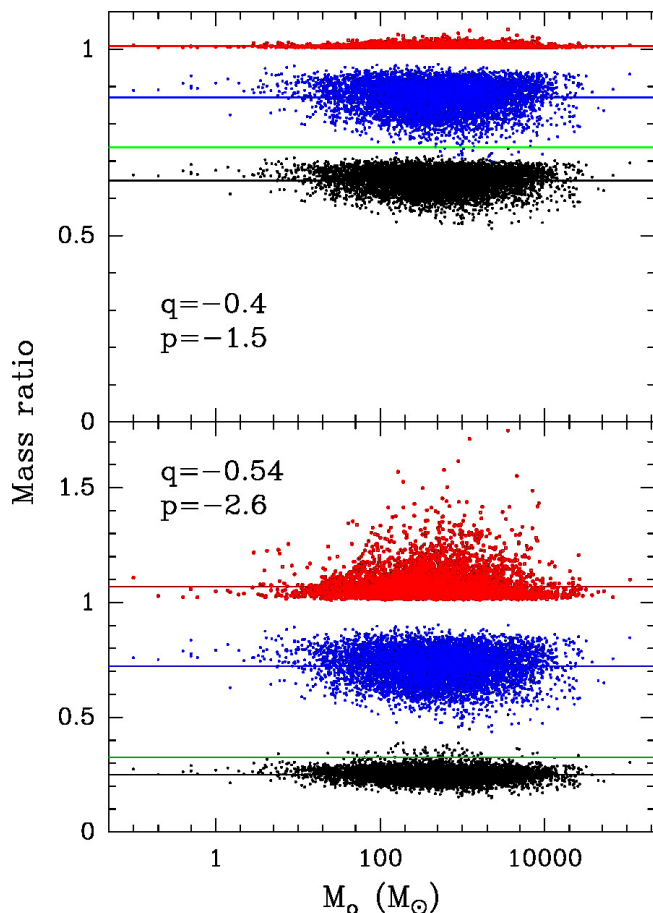


Fig. 8. The black dots indicate the ratio between the mass estimated with our numerical model and that computed by URQ18 for the compact sources identified in the ATLASGAL survey. The input parameters are taken from URQ18. For our estimates, we assumed two template cases: $q = -0.4$, $p = -1.5$ (top panel) and $q = -0.54$, $p = -2.6$ (bottom panel). The red and blue dots indicate, respectively, the contribution of opacity and RJ approximation to the mass ratio, with the horizontal lines denoting the corresponding mean values for the black (0.64 top panel; 0.25 bottom panel), red (1.01 top panel; 1.07 bottom panel) and blue (0.87 top panel; 0.72 bottom panel) dots. The green line is the factor (0.74 top panel; 0.33 bottom panel) taking into account temperature and density gradients (see text for a detailed explanation).

5. Summary and conclusions

We have estimated the continuum emission from a dusty clump with temperature and density gradients, assuming both spherical and cylindrical symmetry. While our toy model assumes power-law profiles for the physical parameters, it must be kept in mind that real clumps are more complex structures where the temperature and density distributions are determined by heating and cooling processes and must obey the laws of fluidodynamics. Also, fragmentation and sub-clumpiness may affect the observed flux densities, especially if coupled to large opacities. Finally,

clumps are enshrouded in more extended, lower density structures whose emission/absorption might affect the measured flux from the clump. All these issues go beyond the scope of our study, which is nonetheless useful to improve on the usual simplified assumption of homogeneous, optically thin clumps.

We provide the reader with approximate analytical expressions (summarized in Table 1) to calculate the flux density as a function of the clump mass and other relevant parameters and, conversely, derive the mass from the measured flux in the optically thin and RJ limits. Also, in Eqs. (20) and (27) we give an approximate solution to the radiative transfer equation to calculate the brightness along an arbitrary line of sight through the clump for any optical depth. Our approach overcomes the problem represented by possibly steep density and temperature gradients at small clump radii. The approximate solution is then used to evaluate the flux density of the core numerically.

Comparison between the numerical and approximate analytical solutions allows to inspect the limits due to the optically thin, Rayleigh-Jeans, and constant-density/temperature approximations. We conclude that in most cases the correction is about a factor 2–3, although in some extreme cases characterised by unusually steep gradients and/or high frequencies, the error introduced by the above approximations can be larger. In order to illustrate all these effects, we have applied our method to three practical examples taken from the literature, demonstrating that the correction to the clump mass may significantly affect the estimate of the clump stability.

Acknowledgements. It is a pleasure to thank Daniele Galli and Maite Beltrán for critically reading the manuscript and useful suggestions.

References

- Beltrán, M. T., Cesaroni, R., Rivilla, R. et al. 2018, A&A, 615, A141 (BEL18)
- Cesaroni, R., Hofner, P., Araya, E., & Kurtz, S. 2010, A&A, 509, A50
- Cesaroni, R., Beltrán, M. T., Moscadelli, L., Sánchez-Monge, Á., & Neri, R. 2019, A&A, 624, A100
- Dyson, J.E. & Williams, D.A. 1980, The Physics of the Interstellar Medium, Manchester University Press, Manchester
- Fontani, F., Cesaroni, R., Caselli, P., & Olmi, L. 2002, A&A, 389, 603 (FON02)
- Hildebrand, R. H. 1983, QJRAS, 24, 167
- MacLaren, I., Richardson, K. R., & Wolfendale, W. 1988, ApJ, 333, 821
- Ossenkopf, V. & Henning, Th. 1991, A&A, 291, 943
- Schuller, A., Menten, K. M., Contreras, Y., et al. 2009, A&A, 504, 415
- Urquhart, J. S., Csengeri, T., Wyrowski, F., et al. 2014, A&A, 568, A41 (URQ14)
- Urquhart, J. S., König, C., Giannetti, A., et al. 2018, MNRAS, 473, 1059 (URQ18)

Appendix A: Function $F(r_i; q, a)$

The purpose of this appendix is to study the behaviour of F defined by Eq. (10) as a function of r_i , in the non-trivial case $q \neq 0$. In the following we consider three possible cases depending on the value of a and demonstrate that F is always increasing with r_i if $q > 0$, and decreasing if $q < 0$.

Appendix A.1: Case $a = 0$

In this case $F(r_i) = (r_i^q - 1)/\ln r_i^q$, which may be conveniently re-written as $F'(y) = (y - 1)/\ln y$ with $y = r_i^q$. The function is to be studied in the range $0 < r_i \leq 1$ or $y > 0$.

First of all we note that

$$\lim_{r_i \rightarrow 0^+} F(r_i) = \begin{cases} \lim_{y \rightarrow 0^+} \frac{-1}{\ln y} = 0 & \Leftrightarrow q > 0 \\ \lim_{y \rightarrow +\infty} \frac{1}{\ln y} = \lim_{t \rightarrow 0^+} \frac{1}{-t \ln t} = +\infty & \Leftrightarrow q < 0 \end{cases}$$

and

$$\lim_{r_i \rightarrow 1^-} F(r_i) = \lim_{y \rightarrow 1} F'(y) = \lim_{t \rightarrow 0} \frac{t}{\ln(1+t)} = 1$$

where we have defined $t = y - 1$. Furthermore, the derivative of $F'(y)$ is equal to

$$\frac{dF'}{dy} = \frac{y \ln y - y + 1}{y(\ln y)^2} = \frac{g(y)}{y(\ln y)^2} \quad (\text{A.1})$$

whose sign is determined by the sign of $g(y) = y \ln y - y + 1$. Since $g(1) = 0$ and $dg/dy = \ln y > 0 \Leftrightarrow y > 1$, we conclude that g has a minimum in $y = 1$ and thus $g \geq 0$ for any $y > 0$. Consequently, $dF'/dy \geq 0$ and $dF/dr_i = q r_i^{q-1} (dF'/dy) > 0 \Leftrightarrow q > 0$.

Appendix A.2: Case $a \neq 0$ and $a = -q$

The result in this case is straightforward. Function $F(r_i) = \ln r_i^a / (r_i^a - 1)$ with $a = -q$ is the inverse of that studied in Sect. A.1, and is thus increasing with r_i if and only if $a < 0$, i.e. for $q > 0$.

Appendix A.3: Case $a \neq 0$ and $a \neq -q$

In this case it is convenient to re-write the function

$$F(r_i) = \frac{a}{a+q} \frac{1 - r_i^{a+q}}{1 - r_i^a} \quad (\text{A.2})$$

assuming $y = r_i^a$ and $b = (a+q)/a$, which gives

$$F'(y) = \frac{1}{b} \frac{1 - y^b}{1 - y} \quad (\text{A.3})$$

For any value of $a \neq 0$, one finds

$$\lim_{r_i \rightarrow 1^-} F(r_i) = \lim_{y \rightarrow 1} F'(y) = \lim_{t \rightarrow 0} \frac{1 - (1+t)^b}{-t} = 1$$

The calculation of the value of F for $r_i = 0$, depends on the sign of a . We obtain for $a > 0$

$$\lim_{r_i \rightarrow 0^+} F(r_i) = \lim_{y \rightarrow 0^+} F'(y) = \begin{cases} \frac{1}{b} & \Leftrightarrow b > 0 \\ +\infty & \Leftrightarrow b < 0 \end{cases}$$

and for $a < 0$

$$\lim_{r_i \rightarrow 0^+} F(r_i) = \lim_{y \rightarrow +\infty} F'(y) = \begin{cases} \lim_{y \rightarrow +\infty} \frac{1}{b} \frac{y^b}{y} = +\infty & \Leftrightarrow b > 1 \\ \lim_{y \rightarrow +\infty} \frac{1}{b} \frac{y^b}{y} = 0 & \Leftrightarrow 0 < b < 1 \\ \lim_{y \rightarrow +\infty} \frac{1}{b} \frac{1}{y} = 0 & \Leftrightarrow b < 0 \end{cases}$$

We note that $b = 0$ and $b = 1$ are excluded because we are considering the case for $a + q \neq 0$ and $q \neq 0$.

In conclusion,

$$\lim_{r_i \rightarrow 0^+} F(r_i) = \begin{cases} 0 & \Leftrightarrow a < 0, q < 0 \\ \frac{a}{a+q} & \Leftrightarrow a > 0, a + q > 0 \\ +\infty & \Leftrightarrow a < 0, q > 0 \text{ or } a > 0, a + q < 0 \end{cases}$$

The derivative of F is $dF/dr_i = ar_i^{a-1} dF'/dy$, where

$$\frac{dF'}{dy} = \frac{1 - by^{b-1}(1-y) + 1 - y^b}{b(1-y)^2} \quad (\text{A.4})$$

so that the sign of dF/dr_i depends on $ag(y)/b$, where we have defined $g(y) = -by^{b-1}(1-y) + 1 - y^b$. We find that $dg/dy = b(b-1)y^{b-2}(y-1) \geq 0$ if $y \geq 1$, for $b(b-1) > 0$, and $y \leq 1$, for $b(b-1) < 0$. This means that g has a minimum in $y = 1$ if $b > 1$ or $b < 0$, a maximum if $0 < b < 1$. Consequently, for any y it is $g \geq 0$ in the former case and $g \leq 0$ in the latter, because in all cases $g(1) = 0$.

Based on the above, one finds that $g/b > 0 \Leftrightarrow b > 1$, so that $dF/dr_i \propto ag/b > 0 \Leftrightarrow a > 0, (a+q)/a > 1$ or $a < 0, (a+q)/a < 1$. Both conditions are equivalent to $q > 0$. We conclude that $F(r_i)$ is a growing function of r_i if and only if $q > 0$. Since $F(1) = 1$, this implies also that $F \geq 1 \Leftrightarrow q < 0$.

Appendix B: Virial mass with density and temperature gradients

We want to derive the expression of the virial mass of a spherically symmetric clump with temperature and density described by Eqs. (2) and (3). The virial theorem can be expressed, e.g., as in Eqs.(8.4) and (8.5) of Dyson & Williams (1980), namely

$$3 \int P dV = \int G \frac{M(R)}{R} dM \quad (\text{B.1})$$

where P is the gas pressure, V the volume, $M(R)$ the mass inside radius R , G the gravitational constant, and we have assumed that the external pressure is null. Using our notation (see Sect. 2), $M(R)$ is obtained by integrating Eq. (8) between R_i and R , i.e.

$$M(R) = \int_{R_i}^R \rho \mathcal{R} 4\pi R'^2 dR' = 4\pi R_0^3 \rho_0 \mathcal{R} \int_{r_i}^r r'^{p+2} dr' \quad (\text{B.2})$$

which can be written as

$$M(R) = M(R_0) \frac{\int_{r_i}^r r'^{p+2} dr'}{\int_{r_i}^1 r'^{p+2} dr'} \quad (\text{B.3})$$

The gas pressure is

$$P(R) = \mathcal{R} \rho(R) \left(\frac{kT(R)}{\mu} + \frac{\sigma_{\text{NT}}^2}{3} \right) \quad (\text{B.4})$$

where μ is the mean mass per particle and σ_{NT} is the velocity dispersion due to microscopic non-thermal motions, which we assume independent of R . The virial mass, M_{vir} , is the value of $M(R_0)$ that satisfies Eq. (B.1), which takes the form

$$\int_{r_i}^1 \left(3\mathcal{R} \rho_0 \frac{kT_0}{\mu} r^{p+q} + \mathcal{R} \rho_0 \sigma_{\text{NT}}^2 r^p \right) R_0^3 4\pi r^2 dr = \int_{r_i}^1 GM_{\text{vir}} \frac{\int_{r_i}^r r'^{p+2} dr'}{\int_{r_i}^1 r'^{p+2} dr'} 4\pi \mathcal{R} \rho_0 R_0^2 r^{p+1} dr \quad (\text{B.5})$$

The solution is

$$M_{\text{vir}} = \frac{\sigma_{\text{NT}}^2 R_0}{G} \int_{r_i}^1 r^{p+2} dr \times \frac{\eta \int_{r_i}^1 r^{p+q+2} dr + \int_{r_i}^1 r^{p+2} dr}{\int_{r_i}^1 \left(\int_{r_i}^r r'^{p+2} dr' \right) r^{p+1} dr} \quad (\text{B.6})$$

where we have defined $\sigma_0^2 = 3kT_0/\mu$ and $\eta = \sigma_0^2/\sigma_{\text{NT}}^2$. Depending on the values of p and q the solution takes the following forms:

$$M_{\text{vir}} = M_{\text{NT}} \times \begin{cases} (\eta + 1) \frac{r_i \ln^2 r_i}{1+r_i \ln r_i - r_i} & \Leftrightarrow p = -3, q = 0 \\ r_i \ln r_i \frac{\ln r_i - \eta \frac{1-r_i^q}{q}}{1+r_i \ln r_i - r_i} & \Leftrightarrow p = -3, q \neq 0 \\ \left(\frac{1-r_i^{p+3}}{p+3} - \eta \ln r_i \right) \frac{1-r_i^{p+3}}{E(r_i, p)} & \Leftrightarrow p \neq -3, q = -p-3 \\ \left(\eta \frac{1-r_i^{p+q+3}}{p+q+3} + \frac{1-r_i^{p+3}}{p+3} \right) \frac{1-r_i^{p+3}}{E(r_i, p)} & \Leftrightarrow p \neq -3, q \neq -p-3 \end{cases} \quad (\text{B.7})$$

where $M_{\text{NT}} = \sigma_{\text{NT}}^2 R_0/G$ and

$$E(r_i, p) = \int_{r_i}^1 (r^{p+3} - r_i^{p+3}) r^{p+1} dr = \begin{cases} -\ln r_i + 2 \frac{r_i^{\frac{1}{2}} - 1}{r_i} & \Leftrightarrow p = -\frac{5}{2} \\ 1 - r_i + r_i \ln r_i & \Leftrightarrow p = -2 \\ \frac{1-r_i^{2p+5}}{2p+5} + \frac{r_i^{2p+5} - r_i^{p+3}}{p+2} & \Leftrightarrow p \neq -\frac{5}{2}, p \neq -2 \end{cases} \quad (\text{B.8})$$

It is possible to demonstrate that if $p \leq -5/2$ or $q \leq -p-3$, for $r_i \rightarrow 0^+$ no equilibrium configuration can be attained, because either the gravitational energy overwhelms the internal energy of the clump ($M_{\text{vir}} \rightarrow 0$) or the opposite happens ($M_{\text{vir}} \rightarrow +\infty$). Vice versa, for $p > -5/2$ and $q > -p-3$ one finds that

$$\lim_{r_i \rightarrow 0^+} M_{\text{vir}} = M_{\text{NT}} (2p+5) \left(\frac{1}{p+3} + \frac{\eta}{p+q+3} \right)$$

which for $\eta = 0$ (i.e. negligible thermal contribution to the internal energy) turns into Eq. (1) of MacLaren et al. (1988)².

The mass M_{NT} can be conveniently expressed in useful units as

$$M_{\text{NT}} = \frac{3(\Delta V)^2 R_0}{8 \ln 2 G} = 125.8 M_\odot [\Delta V(\text{km s}^{-1})]^2 R_0(\text{pc}) \quad (\text{B.9})$$

where the factor 3 takes into account that the observed line full width at half maximum, ΔV , is a measurement of the velocity dispersion along the l.o.s., i.e. in one dimension.

The relevant parameters for the case discussed in Sect. 4.2 are $p = -2.6$, $q = -0.54$, and $r_i = 0.01$, which imply $M_{\text{vir}} \simeq M_{\text{NT}}(1.496\eta + 0.487)$, with $\eta \simeq 0.01647 T_0(\text{K})/[\Delta V(\text{km s}^{-1})]^2$. Here we have assumed $\mu = 2.8 m_{\text{H}}$, with m_{H} mass of the hydrogen atom.

² These authors erroneously state that their equation holds for any $p > -3$, instead of $p > -5/2$.